Generalized algebraic scene-based nonuniformity correction algorithm

Bradley M. Ratliff, Majeed M. Hayat, and J. Scott Tyo

Department of Electrical and Computer Engineering, The University of New Mexico, Albuquerque, New Mexico 87131-1356

Received April 21, 2004; revised manuscript received August 11, 2004; accepted August 11, 2004

A generalization of a recently developed algebraic scene-based nonuniformity correction algorithm for focal plane array (FPA) sensors is presented. The new technique uses pairs of image frames exhibiting arbitrary one- or two-dimensional translational motion to compute compensator quantities that are then used to remove nonuniformity in the bias of the FPA response. Unlike its predecessor, the generalization does not require the use of either a blackbody calibration target or a shutter. The algorithm has a low computational overhead, lending itself to real-time hardware implementation. The high-quality correction ability of this technique is demonstrated through application to real IR data from both cooled and uncooled infrared FPAs. A theoretical and experimental error analysis is performed to study the accuracy of the bias compensator estimates in the presence of two main sources of error. © 2005 Optical Society of America

OCIS codes: 100.2000, 100.2550, 100.3020, 110.3080, 110.4280.

1. INTRODUCTION

Fixed pattern noise, or spatial nonuniformity, is a well-known problem in focal plane array (FPA) sensors.[1] This noise is particularly problematic for midwave infrared (MWIR) and long-wave infrared (LWIR) array imagers.[2] Spatial nonuniformity is a difficult problem to remedy, as it is known to change slowly in time, thus requiring repeated estimation and removal of the nonuniformity in order to achieve clean, temperature-accurate imagery. Traditionally, nonuniformity correction (NUC) has been performed with calibration techniques that require frequent obstruction of the camera's field of view with a blackbody calibration target. This target is usually heated to multiple temperatures, yielding spatially constant temperature images. The gain and the bias can be extracted from these flat images by employing a linear (or higher-order) fit, and the nonuniformity is thus compensated for.[3]

Recent research has focused on the development of scene-based NUC algorithms. The motivation behind these techniques is to eliminate the cost and the complexity associated with blackbody calibration systems, particularly in applications where radiometry is of no concern. Such techniques nonobstructively estimate and remove nonuniformity at the cost of compromising radiometric accuracy. A major sector of scene-based techniques is statistical in nature; i.e., the algorithms require certain (and sometimes strict) spatiotemporal statistical assumptions on the imaged scene, which typically require long sequences of imagery to be fulfilled. Statistical algorithms include those by Narendra and Foss,[4,5] Harris and Chiang,[6,7] Hayat *et al.*,[8] and Torres and Hayat.[9] When these statistical assumptions are violated, the resulting algorithm performance is poor. For example, the constant-statistic assumption[4–7] is problematic when motion in the image sequence is not sufficiently diverse to ensure that the irradiance statistics at each pixel are uniform across the array. Moreover, many of these techniques typically require a significant number of image frames in order to obtain a reasonable NUC. The algorithms can require thousands of frames under certain spatial distributions and levels of motion.

Registration-based techniques constitute another class of scene-based NUC algorithms and exploit precise knowledge of interframe global motion to estimate the "flow" of irradiance in space and use it as a basis for extracting the bias nonuniformity. Two such techniques are those developed by O'Neil,[10–12] which require predetermined whole-pixel camera motion, and that of Hardie *et al.*,[13] which relies on whole-pixel motion estimation. These algorithms estimate the nonuniformity in hundreds of frames instead of thousands at the cost of higher computational complexity due to their need for motion estimation or induced motion.

For its relevance to this paper, we now focus on a class of registration-based algorithms that was recently developed by Ratliff *et al.*[14,15] The so-called algebraic scene-based algorithm (ASBA)[14] uses image pairs that exhibit subpixel one-dimensional (1D) translational motion, i.e., purely vertical and purely horizontal shifts less than 1 pixel in magnitude, to unify the detector biases across the entire array to that of a single common bias value. The technique was later extended by the authors to a radiometrically accurate form (RASBA) that accommodates arbitrary, subpixel or superpixel two-dimensional (2D) global motion.[15] This extension was achieved by employing a limited perimeter-only blackbody calibration system that absolutely calibrates detectors along the perimeter of the FPA while leaving interior detectors unobstructed. The corrected imagery resulting from this technique is radiometrically accurate in the sense that all of the pixels—not just the calibrated perimeter pixels—have zero bias. The RASBA technique enjoys the nonobstructive advantage of scene-based algorithms while yielding the radio-

metric benefit of calibration techniques. To our knowledge, this is the first technique to successfully bridge calibration- and scene-based techniques.

The goal of this paper is to generalize the concept of the earlier nonradiometric algebraic algorithm (i.e., ASBA) to a form that is capable of utilizing arbitrary 1D *or* 2D global motion, i.e., shifts containing both a horizontal and a vertical motion component with magnitudes larger than 1 pixel. This extension is achieved by (1) unifying the bias values of detectors along the perimeter to a single unknown bias value through application of the ASBA, and (2) once perimeter uniformity has been accomplished, by applying a new version of the RASBA algorithm that does *not* require calibration of the perimeter detectors. In the RASBA technique, absolute calibration of the perimeter detectors effectively sets all the biases of the perimeter detectors to zero. In this work, we relax this calibration constraint to require only that all perimeter detectors be free from bias nonuniformity, in which case perimeter detector biases are not required to be zero but instead must have a common, unknown value. Thus, in applications where absolute radiometric accuracy is not necessary, this generalized algebraic scene-based algorithm (GASBA) allows for removal of the nonuniformity in practically all cases where a video sequence is available with global translational motion. Consequently and more importantly, the performance of the GASBA is significantly better than that of the ASBA technique, removing image artifacts such as horizontal or vertical striping that were observed in the original ASBA corrections.

This paper is organized as follows. In Section 2, we provide a brief review of the RASBA technique and present its nonradiometric-mode generalization, namely, the GASBA. Section 3 is devoted to the algorithm's application to real IR data. A theoretical and experimental error analysis is performed in Section 4 that addresses the effects of errors due to bilinear interpolation (utilized by our algorithm to model motion) and nonideal bias correction of the perimeter detectors. Finally, the conclusions are contained in Section 5.

2. ALGORITHM DESCRIPTION

The GASBA technique consists of two main stages: an initialization stage and a lock-in stage. In the initialization stage, the ASBA technique is applied to pairs of images (from a video sequence) that are identified to exhibit 1D subpixel shifts. The ASBA is capable of quickly (but roughly) unifying the bias values of the entire FPA to a common bias value. We use this capability to unify the bias values in only those pixels that are along perimeter rows and columns of the FPA. Thus the initialization stage serves to provide a rough unification of the perimeter biases that is achievable even in cases for which the population of the 1D subpixel-shifted image pairs in the image sequence is small. We use this initial bias unification as a starting point for the lock-in stage. In the lock-in stage, we use the remaining image pairs in the sequence that contain arbitrary 2D motion, which typically form the majority of the shifted pairs, to obtain a far more robust NUC. This is accomplished by the new nonradiometric form of the RASBA technique (detailed in Subsection 2.B).

A. Review of the Radiometrically Accurate Algebraic Scene-Based Algorithm

We begin by reviewing germane aspects of the original RASBA technique. We include the necessary portions of the RASBA here for completeness, but for a more thorough discussion we refer the reader to our earlier work.[15] Consider an image sequence y_k generated by an $M \times N$ FPA, where $k = 1,2,...$ represents the image frame number. The maximum translational shift between consecutive image frames that can be used by the RASBA algorithm is set to the width of the calibrated perimeter, which is determined by the calibration system. This upper bound on the shift is denoted by L (pixels). We will assume henceforth that all image pairs satisfy the L-shift upper bound condition. We work under the assumption that the dominant source of fixed-pattern noise is detector bias. (Although this assumption is justified in most cases of interest, we demonstrate in Section 3 that the algorithm works well even in cases where gain nonuniformity is present.) Thus we approximate the output of an (i, j)th detector at time k by the linear model

$$y_k(i, j) = z_k(i, j) + b(i, j), \tag{1}$$

where the quantity $z_k(i, j)$, termed here as the signal, is proportional to the number of IR photons collected by the (i, j)th detector during the camera integration time and $b(i, j)$ is the detector bias, where $i = 1,2,...,M$ and $j = 1,2,...,N$.

We will assume throughout that the radiation emanating from the scene (both emitted and reflected) does not change significantly during the time between image frames. Thus when two image frames exhibit an arbitrary translational motion between them, we approximate the signal at a given pixel in the $(k + 1)$th frame as a bilinear interpolation of the signals corresponding to the appropriate four pixels from the kth frame. This is done as follows: Let α_k and β_k be the vertical and horizontal components of the shift between the kth and $(k + 1)$th images, respectively. Further, let us write these shifts as the sum of their whole-integer and fractional parts, i.e., $\alpha_k = \lfloor \alpha_k \rfloor + \Delta\alpha_k$ and $\beta_k = \lfloor \beta_k \rfloor + \Delta\beta_k$, where $\lfloor \cdot \rfloor$ indicates the integer part of the shift. For convenience, we define the fractional areas $\gamma_{1,k} = |\Delta\alpha_k \Delta\beta_k|$, $\gamma_{2,k} = (1 - |\Delta\alpha_k|)|\Delta\beta_k|$, $\gamma_{3,k} = |\Delta\alpha_k|(1 - |\Delta\beta_k|)$, and $\gamma_{4,k} = (1 - |\Delta\alpha_k|)(1 - |\Delta\beta_k|)$. Note that $\gamma_{1,k} + \gamma_{2,k} + \gamma_{3,k} + \gamma_{4,k} = 1$. For simplicity, assume that the shift is in the down-rightward direction and corresponds to our convention that $\alpha_k > 0$ and $\beta_k > 0$. With this notation, the bilinear-interpolation approximation $\hat{z}_{k+1}(i, j)$ for the signal $z_{k+1}(i, j)$ becomes

$$\begin{aligned} \hat{z}_{k+1}(i, j) = {} & \gamma_{1,k} z_k(i - \lfloor \alpha_k \rfloor - 1, j - \lfloor \beta_k \rfloor - 1) \\ & + \gamma_{2,k} z_k(i - \lfloor \alpha_k \rfloor, j - \lfloor \beta_k \rfloor - 1) \\ & + \gamma_{3,k} z_k(i - \lfloor \alpha_k \rfloor - 1, j - \lfloor \beta_k \rfloor) \\ & + \gamma_{4,k} z_k(i - \lfloor \alpha_k \rfloor, j - \lfloor \beta_k \rfloor). \end{aligned} \tag{2}$$

By substituting the above interpolation model for the signal into Eq. (1), we obtain a bilinearly interpolated approximation for the $(k+1)$th detector output in terms of the signal's spatial distribution in the previous frame. More precisely, if we neglect the interpolation error by assuming that $\hat{z}_{k+1}(i,j) = z_{k+1}(i,j)$, then for $i = 2 + \lfloor \alpha_k \rfloor, 3 + \lfloor \alpha_k \rfloor, \ldots, M$ and $j = 2 + \lfloor \beta_k \rfloor, 3 + \lfloor \beta_k \rfloor, \ldots, N$, we obtain

$$\begin{aligned} y_{k+1}(i,j) = {} & \gamma_{1,k} z_k(i - \lfloor \alpha_k \rfloor - 1, j - \lfloor \beta_k \rfloor - 1) \\ & + \gamma_{2,k} z_k(i - \lfloor \alpha_k \rfloor, j - \lfloor \beta_k \rfloor - 1) \\ & + \gamma_{3,k} z_k(i - \lfloor \alpha_k \rfloor - 1, j - \lfloor \beta_k \rfloor) \\ & + \gamma_{4,k} z_k(i - \lfloor \alpha_k \rfloor, j - \lfloor \beta_k \rfloor) + b(i,j). \end{aligned} \tag{3}$$

This signal interpolation model is depicted in Fig. 1(a).

The key step in the RASBA technique is to compute the so-called bias differential $\Delta_k(i,j)$ for each nonperimeter detector. This bias differential is calculated from the image sequence as follows[15]:

$$\begin{aligned} \Delta_k(i,j) = {} & \gamma_{1,k} y_k(i - \lfloor \alpha_k \rfloor - 1, j - \lfloor \beta_k \rfloor - 1) \\ & + \gamma_{2,k} y_k(i - \lfloor \alpha_k \rfloor, j - \lfloor \beta_k \rfloor - 1) \\ & + \gamma_{3,k} y_k(i - \lfloor \alpha_k \rfloor - 1, j - \lfloor \beta_k \rfloor) \\ & + \gamma_{4,k} y_k(i - \lfloor \alpha_k \rfloor, j - \lfloor \beta_k \rfloor) - y_{k+1}(i,j). \end{aligned} \tag{4}$$

When we substitute Eqs. (1) and (3) into Eq. (4), we find that

$$\begin{aligned} \Delta_k(i,j) = {} & \gamma_{1,k} b(i - \lfloor \alpha_k \rfloor - 1, j - \lfloor \beta_k \rfloor - 1) \\ & + \gamma_{2,k} b(i - \lfloor \alpha_k \rfloor, j - \lfloor \beta_k \rfloor - 1) \\ & + \gamma_{3,k} b(i - \lfloor \alpha_k \rfloor - 1, j - \lfloor \beta_k \rfloor) \\ & + \gamma_{4,k} b(i - \lfloor \alpha_k \rfloor, j - \lfloor \beta_k \rfloor) - b(i,j). \end{aligned} \tag{5}$$

With the above preliminaries, the bias-correction capability of the RASBA can be described as follows. Suppose that we calibrate the topmost L rows and leftmost L columns of detectors such that we force each perimeter detector to have a unity gain and a zero bias. We then observe that for the top-leftmost uncalibrated detector, i.e., for $i = L+1$ and $j = L+1$, the differential bias $\Delta_k(L+1, L+1)$ is precisely equal to $-b(i,j)$, since all of the γ-scaled bias terms are equal to zero on account of calibration. Hence we define the first bias compensator corresponding to the kth frame pair as $c_k(L+1, L+1) \triangleq -\Delta_k(L+1, L+1)$. To compute the bias compensators in general, we must transform each $\Delta_k(i,j)$ term in Eq. (5) into the desired $-b(i,j)$ form. Thus the (i,j)th bias compensator is obtained by progressively updating $\Delta_k(i,j)$ according to

$$\begin{aligned} c_k(i,j) = {} & \Delta_k(i,j) + \gamma_{1,k} c_k(i - \lfloor \alpha_k \rfloor - 1, j - \lfloor \beta_k \rfloor - 1) \\ & + \gamma_{2,k} c_k(i - \lfloor \alpha_k \rfloor, j - \lfloor \beta_k \rfloor - 1) \\ & + \gamma_{3,k} c_k(i - \lfloor \alpha_k \rfloor - 1, j - \lfloor \beta_k \rfloor) \\ & + \gamma_{4,k} c_k(i - \lfloor \alpha_k \rfloor, j - \lfloor \beta_k \rfloor). \end{aligned} \tag{6}$$

Clearly, the algorithm has a spatially recursive structure. The recursion starts with the top-leftmost uncalibrated detector and proceeds in a down-rightward manner, updating one row or column of the bias differentials at a time. Each bias compensator is progressively estimated in this way until all array indices have been exhausted. Note that the calibrated detectors of the perimeter provide the boundary conditions required to begin this recursive process. Finally, because the bias compensators are estimated for k image pairs, we average these k estimates for each (i,j)th detector to reduce the effects of estimation error (discussed formally in Section 4). Having explained these central ideas, we next present the generalized form of the RASBA technique.

B. Description of the Generalized Algorithm

Instead of using the perimeter calibration system to unify the L perimeter rows and columns, we now employ the ASBA technique to perform an initial bias unification of the perimeter detectors. In doing so, we are no longer restricted to a fixed perimeter size, but instead our upper bound L is limited only by the accuracy of the shift estimator (for the shift estimation algorithm[16] that we employed, $L = 30$ pixels). Thus the perimeter size can be dynamically selected for each image pair; therefore, for each image pair, we unify the biases of the topmost $\lfloor \alpha_k \rfloor + 1$ rows and leftmost $\lfloor \beta_k \rfloor + 1$ columns (but not to exceed L). Next, given a 2D shifted pair of perimeter-unified images, we apply the RASBA algorithm as described in Subsection 2.A.

To show that application of the RASBA to these perimeter-unified images will indeed unify all detectors in the FPA to a single bias value b, we first compute the bias compensator for detector $(2 + \lfloor \alpha_k \rfloor, 2 + \lfloor \beta_k \rfloor)$. Note that in this case the computation of the bias differential involves direct use of the perimeter detectors. Thus the bias differential is

$$\begin{aligned} \Delta_k(2 + \lfloor \alpha_k \rfloor, 2 + \lfloor \beta_k \rfloor) = {} & \gamma_{1,k} b + \gamma_{2,k} b + \gamma_{3,k} b + \gamma_{4,k} b \\ & - b(2 + \lfloor \alpha_k \rfloor, 2 + \lfloor \beta_k \rfloor). \end{aligned} \tag{7}$$

Since the γ terms sum to unity, Eq. (7) becomes

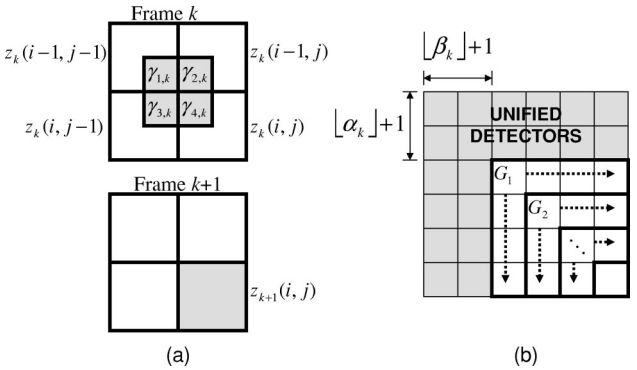

Fig. 1. (a) Depiction of the bilinear signal interpolation model for the case of subpixel 2D motion. The shaded pixels represent the interpolated signal value at time $k+1$. (b) Representation of the recursive operation of the algorithm. The pixel partitions in bold outline correspond to each G_l, representing the group of detectors whose biases are estimated iteratively in l. The arrows indicate the direction of algorithm iteration within each G_l.

$$\Delta_k(2 + \lfloor \alpha_k \rfloor, 2 + \lfloor \beta_k \rfloor) = b - b(2 + \lfloor \alpha_k \rfloor, 2 + \lfloor \beta_k \rfloor). \tag{8}$$

Clearly, if this bias differential is added to the top-leftmost nonunified detector output $y(2 + \lfloor \alpha_k \rfloor, 2 + \lfloor \beta_k \rfloor)$, its bias will be subtracted and replaced with a value of b, hence unifying this detector's bias to that of the perimeter. In this case, the bias differential is automatically of the desired form. In general, when detectors are sufficiently far from the perimeter [i.e., for detectors with indices $i > 2(2 + \lfloor \alpha_k \rfloor)$ and $j > 2(2 + \lfloor \beta_k \rfloor)$] the bias differentials are of the general form given in Eq. (5). To transform these bias differentials to the desired form of Eq. (8), we apply a recursive update procedure similar to the RASBA, which is now described.

The entire GASBA technique is formalized below. To ease this description, it is convenient to first partition the nonperimeter pixels as follows. For $\min(2 + \lfloor \alpha_k \rfloor, 2 + \lfloor \beta_k \rfloor) \leqslant l \leqslant \min(M, N)$, define G_l to represent the group of pixels consisting of $\{(l, l),\ldots,(M, l), (l, l + 1),\ldots,(l, N)\}$, as depicted in Fig. 1(b) (note that l depends on k). Next, we organize all images in the sequence into pairs of adjacent image frames and denote each pair by I_k. Further, we define the image-pair set S_1 as the collection of all image pairs exhibiting 1D subpixel shifts and the set S_2 as the collection of all image pairs exhibiting 2D subpixel and superpixel shifts, with the proviso that the maximum shift has an integral part no greater than L. Given these definitions, the GASBA is then summarized as follows:

1. Estimate the motion vector (α_k, β_k) for each I_k. Then place each I_k in the appropriate group, namely, S_1 or S_2, according to its motion estimate.
2. *Initialization stage*: Extract the initial bias nonuniformity compensators by employing the ASBA technique in conjunction with the sequence S_1.
3. For each $I_k \in S_2$, unify the perimeter bias values, i.e., for $i = 1,\ldots,M$, $j = 1,\ldots,\lfloor \beta_k \rfloor + 1$ and $i = 1,\ldots,\lfloor \alpha_k \rfloor + 1$, $j = \lfloor \beta_k \rfloor + 2,\ldots,N$, by using the ASBA bias compensators calculated in the previous step. The perimeter thickness does not exceed L pixels.
4. *Lock-in stage*: For each k for which $I_k \in S_2$, compute the bias differentials $\Delta_k(i, j)$ in G_l for all l according to Eq. (4).
5. Update the bias differentials, resulting in the bias compensators $c_k(i, j)$ for each k, by using the following recursive procedure:
   (a) Start the recursion: Put $l = \min(2 + \lfloor \alpha_k \rfloor, 2 + \lfloor \beta_k \rfloor)$ and estimate the bias compensators in G_l according to Eq. (6).
   (b) For each k for which $I_k \in S_2$, calculate the bias compensators $c_k(i, j)$ in G_{l+1} according to Eq. (6) for $(i, j) \in G_{l+1}$.
   (c) Repeat the previous step and terminate the recursion when $l = 1 + \min(M, N)$.
6. Obtain the final bias compensators by computing the temporal average $c(i, j)$ of the bias compensator $c_k(i, j)$ over all image pairs $I_k \in S_2$.

Note that for any image pair I_k used in step 5(b) above, the bias compensator $c_k(i, j)$ is ideally of the form $c_k(i, j) = b - b(i, j)$, where the b term is the unknown perimeter bias value and is common to all the bias compensators. However, because of factors such as the bilinear-interpolation approximation and the presence of residual perimeter nonuniformity in the initialization stage, there will be some deviation from this ideal behavior. The temporal averaging in the final step above is intended to reduce this error. These errors will be discussed thoroughly in Section 4.

Note that if $b = 0$ (as in the case of the RASBA with perimeter calibration), the GASBA simply collapses to the RASBA.

3. ALGORITHM PERFORMANCE: APPLICATION TO REAL IR DATA

In this section, we employ real IR data to demonstrate the algorithm's ability to accurately remove the nonuniformity.

The GASBA was applied to real IR data. Data set 1 was collected with a cryogenically cooled Amber 128 × 128 12-bit MWIR InSb camera. Figure 2(a) shows the raw camera-outputted image frame 325 from this 512-frame image sequence. Note the high degree of spatial nonuniformity present. For comparison, the data sequence was first corrected with the ASBA and RASBA techniques. The resulting images from these corrections are displayed in Figs. 2(b) and 2(c), respectively. Note the residual vertical striping remaining in the ASBA image. As we alluded to in Section 1, this phenomenon is typical of the ASBA and essentially results from all shifts being one dimensional, i.e., all corrections are performed strictly down rows and across columns. In the RASBA-corrected image, however, we note that these artifacts are not present. In this case, the perimeter ($L = 5$) was unified through a two-point-calibration process, using flat images at 18 °C and 30 °C, to set all biases to zero and gains to unity. Consequently, the resulting imagery would be radiometrically accurate if it were expressed in units of radiance.[15] Note that to get an accurate temperature profile, we would need additional information about the object emissivity and atmospheric properties.

The GASBA-corrected image, shown in Fig. 2(d), is also free from the striping artifacts. In the initialization stage of the GASBA, the bias nonuniformity estimates from the ASBA technique were first applied to the perimeter detectors (recall that in the GASBA the perimeter size is dynamic and thus changes according to the magnitude and the direction of each image-pair shift). Then, in the lock-in stage, the modified RASBA was applied to interior detectors. It is important to note that, because of its tolerance of the striping artifacts in the perimeter, the performance of the GASBA is significantly better than that of the ASBA alone. This is attributable to its utilization of 2D shifted frames.

In the examples above, the number of image pairs used by each algorithm is as follows: The ASBA technique used 107 1D image pairs, the RASBA technique used 44 2D image pairs, and the GASBA used 107 1D image pairs and 44 2D image pairs. Note that the RASBA does not use any 1D image pairs in the correction because the 1D shifted images tend to degrade the accuracy of the bias compensators by introducing the usual striping artifacts.

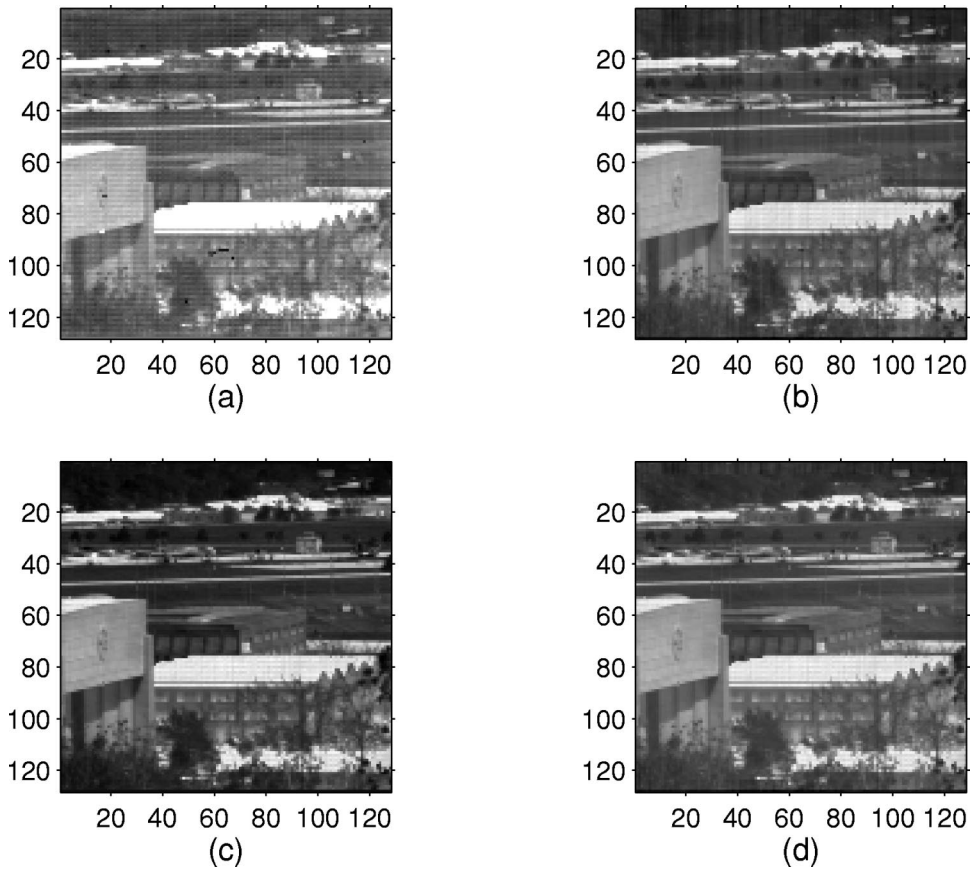

Fig. 2. Image frame 325 from data set 1: (a) raw image, (b) after correction by the ASBA, (c) after correction by the RASBA, (d) after correction by the GASBA. All images are statistically scaled to the same dynamic range.

Also, the 1D image pairs are not needed for initialization, since this is achieved through absolute calibration. The GASBA only uses the 1D image pairs to obtain the bias compensators for the initialization stage. Then, similar to the RASBA, the GASBA uses only the 2D image pairs to estimate the compensators in the array interior. The fact that better corrections are obtained when using 2D shifted image pairs will be theoretically justified in Section 4.

The GASBA was also applied to two sets of 2000-frame data sequences (referred to as data sets 2 and 3), collected approximately 30 min apart and obtained from an uncooled 320×240 LWIR amorphous-silicon microbolometer FPA. The raw uncorrected image frame 320 from data set 2 is displayed in Fig. 3(a). The resulting GASBA-corrected image is displayed in Fig. 3(b). Note that before correction most of the image is obscured by the nonuniformity. After correction, the nonuniformity has been removed, yielding a significant increase in image clarity. The image sequence depicts an indoor scene containing a doorway. In a similar correction for data set 3, Figs. 3(c) and 3(d) show the raw and GASBA-corrected image frame 585, which depicts a VCR unit. The quality of the NUC provided by the algorithm is again apparent. Note that the VCR cord on the right side of the image is not readily distinguishable from the background in the raw image but is clearly seen after correction. It is important to note that the camera used for this experiment was equipped with a mechanical shutter-based calibration system (which performs a one-point calibration). Moreover, the raw images of Fig. 3 have already been calibrated by this shutter-based system. However, for this particular camera, the nonuniformity drift rate was abnormally fast, making the unit unacceptable for customer distribution. Despite the significant level of nonuniformity present, the GASBA was capable of improving the image quality to an acceptable level of performance, in our opinion.

It should be noted that the above corrections are representative of the algorithm in all cases where a video sequence is available with sufficiently diverse translational motion, i.e., when the video sequence contains many frame pairs exhibiting multidirectional motion, both subpixel and superpixel. Furthermore, it was known that the above image sequences contained a significant amount of gain nonuniformity. Despite this fact, the algorithm was able to perform well. This ability of the algorithm will be studied in future work.

4. ERROR ANALYSIS

In this section, we investigate two significant sources of error and study how they affect the accuracy of the bias compensators produced by the algorithm. We focus in particular on the error resulting from our bilinear-interpolation approximation for the shifted signal and the

error resulting from residual nonuniformity in the imagery perimeter during the initialization stage of the GASBA.

We define the bilinear interpolation error for the (i, j)th detector as

$$\epsilon_{\mathrm{BI},k}(i, j) = z_{k+1}(i, j) - \hat{z}_{k+1}(i, j), \tag{9}$$

where $z_{k+1}(i, j)$ is the signal at time $k + 1$ and $\hat{z}_{k+1}(i, j)$ is defined in Eq. (2). These errors become nonzero, for example, as a result of phenomena such as local object motion, dead pixels, geometric distortions (due to relative movement in near-field/far-field objects), object deformation, significant temperature fluctuation of scene objects from frame to frame, and pixel fill fractions in high-frequency data. The most important factor here is that the bilinear interpolation is inaccurate when the imager's spatial resolution is not high enough to capture an object's level of detail, i.e., when an object's detail is smaller than 1 pixel.

The residual nonuniformity error is the deviation of the bias compensators that are produced during the initialization stage by the ASBA technique from their ideal value of $b - b(i, j)$, i.e.,

$$c_{\mathrm{ASBA}}(i, j) = b - b(i, j) + \epsilon_{\mathrm{RN}}(i, j). \tag{10}$$

Note that because these ASBA compensators are applied to the perimeter, each $\epsilon_{\mathrm{RN}}(i, j)$ is defined only for these detectors. Therefore, for the nonperimeter detectors (i.e., for $i = 2 + \lfloor \alpha_k \rfloor, \ldots, M$ and $j = 2 + \lfloor \beta_k \rfloor, \ldots, N$), we define $\epsilon_{\mathrm{RN}}(i, j) = 0$.

Because of the above errors, each bias compensator estimate $c_k(i, j)$ can be cast as

$$c_k(i, j) = b - b(i, j) + \epsilon_{c_k}(i, j) \tag{11}$$

for all i and j. In the following subsections, we present analytical expressions for each $\epsilon_{c_k}(i, j)$ in terms of $\epsilon_{\mathrm{BI},k}(i, j)$ and $\epsilon_{\mathrm{RN}}(i, j)$ for the 1D and 2D, subpixel and superpixel modes of the algorithm. To generate each analytical error expression, we simply substitute the above error models into the appropriate GASBA equation and proceed to compute each bias compensator in the presence of these errors. In particular, we carry out the steps in deriving the algorithm by appending the error term $\epsilon_{\Delta_k}(i, j)$ to Eq. (5), where

$$\begin{aligned}\epsilon_{\Delta_k}(i, j) = {} & \gamma_{1,k}\epsilon_{\mathrm{RN}}(i - \lfloor \alpha_k \rfloor - 1, j - \lfloor \beta_k \rfloor - 1) \\ & + \gamma_{2,k}\epsilon_{\mathrm{RN}}(i - \lfloor \alpha_k \rfloor, j - \lfloor \beta_k \rfloor - 1) \\ & + \gamma_{3,k}\epsilon_{\mathrm{RN}}(i - \lfloor \alpha_k \rfloor - 1, j - \lfloor \beta_k \rfloor) \\ & + \gamma_{4,k}\epsilon_{\mathrm{RN}}(i - \lfloor \alpha_k \rfloor, j - \lfloor \beta_k \rfloor) + \epsilon_{\mathrm{BI},k}(i, j).\end{aligned} \tag{12}$$

Our main focus then is to study how these error terms propagate into the bias compensators through the recursive update procedure.

A. Error Expressions for the Cases of One-Dimensional Motion

For the case of subpixel 1D motion, a straightforward calculation yields that the error present in the (i, j)th bias compensator is

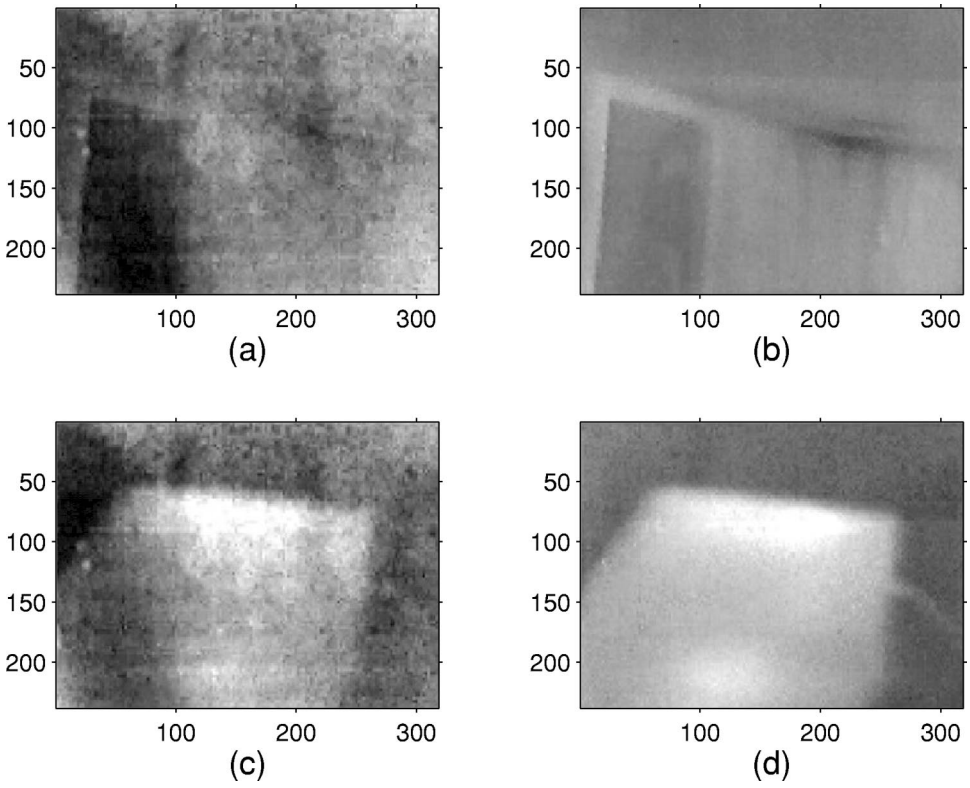

Fig. 3. Imagery from data set 2: (a) raw image frame 320, (b) image frame 320 after correction by the GASBA. Imagery from data set 3: (c) raw image frame 585, (d) image frame 585 after correction by the GASBA. All images are statistically scaled to the same dynamic range.

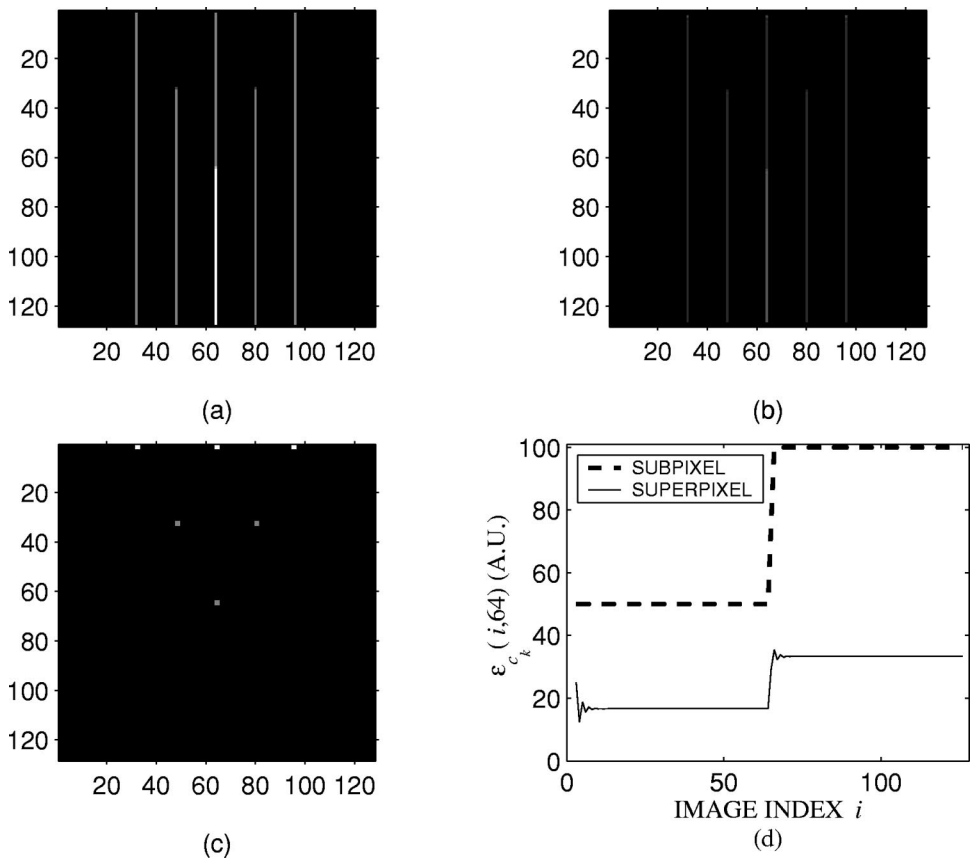

Fig. 4. Propagation of error: (a) subpixel 1D motion case for a shift of (0, 0.5), (b) superpixel 1D motion case for a shift of (0, 1.5), (c) frame 1 of the test pattern image pair (the bright pixels indicate the nonzero values used to introduce residual nonuniformity and bilinear-interpolation error), (d) plot of column 64 for the images in (a) and (b).

$$\epsilon_{c_k}(i,j) = -\frac{1}{|\Delta\alpha_k|}\sum_{m=2}^{i}\epsilon_{\Delta_k}(m,j). \tag{13}$$

Thus we see that the error in a given bias compensator is equal to the summation of all previous $\epsilon_{\Delta_k}(m,j)$ terms, each scaled by $1/|\Delta\alpha_k|$. Clearly, since $|\Delta\alpha_k| < 1$, each $\epsilon_{\Delta_k}(m,j)$ term is amplified as it propagates spatially. Recall that striping artifacts across rows and down columns were common in the corrections produced by the ASBA [as seen in Fig. 2(b)]. The source of these striping artifacts is clearly demonstrated by the error expression of Eq. (13).

The (i,j)th bias compensator error for the 1D superpixel case is

$$\epsilon_{c_k}(i,j) = -\sum_{m=2+\lfloor\alpha_k\rfloor}^{i}\sum_{l=0}^{i-m}\epsilon_{\Delta_k}(m,j)(-|\Delta\alpha_k|)^l. \tag{14}$$

Note that the $\Delta\alpha_k$ terms now appear in the numerator and that each $\epsilon_{\Delta_k}(m,j)$ is multiplied by powers of $-|\Delta\alpha_k|$. Therefore we see that the error is less severe than the error in the 1D subpixel case because of the alternating sign of the factor $(-|\Delta\alpha_k|)^l$, which reduces the error accumulation along rows and columns.

We next experimentally demonstrate how the errors are propagated across the bias compensator estimates for the 1D cases. To do so, we create a pair of images containing a test pattern that introduces both bilinear interpolation and residual perimeter nonuniformity error into the bias compensators. The test images are fabricated by first creating two constant images. Clearly, if the algorithm is applied to these flat images, all bias compensators produced by the algorithm will be zero, as expected. Next, in the first test image, we set specific pixels to nonzero values to introduce bilinear-interpolation and residual nonuniformity errors. The GASBA is then applied to this test image pair. Then, because we expect all bias compensators to have a value of zero, any nonzero compensator values may be attributed to the above two errors.

Figures 4(a) and 4(b) depict the bias compensator estimates generated by the algorithm using the test pattern image pair of Fig. 4(c) for the 1D subpixel and superpixel cases, respectively. In the first test pattern image, residual nonuniformity error was introduced by setting selected pixels along the perimeter to a value of 50 [in arbitrary units (A.U.)], and bilinear-interpolation error was introduced by setting selected interior pixels to a value of 25. All other pixels were set to a value of zero in both test images. Shifts of (0, 0.5) and (0, 1.5) pixels were assumed by the GASBA for the subpixel and superpixel cases, respectively. Figures 4(a) and 4(b) are scaled to the same dynamic range of [0, 100], where the respective ranges of the bias compensators are [0, 100] and [0, 35.4].

Of particular interest is column 64 of each bias compensator image, which is plotted for both cases in Fig. 4(d). For the subpixel case, the error is projected in a stair-step

fashion and is consistent with the error expression of Eq. (13). The superpixel case, on the other hand, is similar in shape but significantly less in magnitude. Also, note the ringing effect near the step edges, corresponding to the alternating sums of Eq. (14). It is important to note that the nonzero test pattern image values were chosen to clearly illustrate the shapes of the error envelopes. In general, this performance will scale with the size of the error. With the source of the 1D-motion striping artifacts understood, we next perform a similar analysis for the 2D-motion cases.

B. Error Expressions for the Cases of Two-Dimensional Motion

For the case of subpixel 2D motion, the (i, j)th bias compensator error is

$$\epsilon_{c_k}(i, j) = -\sum_{m=2}^{i}\sum_{n=2}^{j}\sum_{l=0}^{\min(p,q)} A(p, q, l)\epsilon_{\Delta_k}(m, n) \times \frac{\gamma_{1,k}^{l}\gamma_{2,k}^{p-l}\gamma_{3,k}^{q-l}}{(1-\gamma_{4,k})^{p+q-l+1}}, \tag{15}$$

where $p = i - m$, $q = j - n$, and

$$A(p, q, l) = \frac{(p+q-l)!}{l![p+q-l-\max(p, q)]![\max(p, q)-l]!}. \tag{16}$$

The derivation and the interpretation of the error coefficient term $A(p, q, l)$ are lengthy and will be omitted here. The formal proof relies on a combinatoric argument and the formula for the number of paths in a certain directed graph and will be reported elsewhere. Note that in this case $\epsilon_{c_k}(i, j)$ contains $\epsilon_{\Delta_k}(m, n)$ terms from all nonperimeter detectors above and to the left of it (i.e., $2 \leq m \leq i$ and $2 \leq n \leq j$). Thus we see that the error is spread among a large number of pixels rather than being concentrated solely along rows or columns. Since the γ terms are related to the shift magnitudes, we find that they have the largest magnitudes along the direction of motion. For example, a shift of $\alpha_k = 0.5$ and $\beta_k = 0.5$ will cause the γ terms to be strongest along a direction of $-45°$. Though each $\epsilon_{c_k}(i, j)$ involves many $\epsilon_{\Delta_k}(m, n)$ terms, we find that the error is less severe than in the 1D cases, as the errors tend to damp out as p and q become large. This is due to the fact that the γ terms increase in power (and thus decrease in magnitude) as m and n become sufficiently far from i and j.

The (i, j)th bias compensator error for the 2D superpixel case is

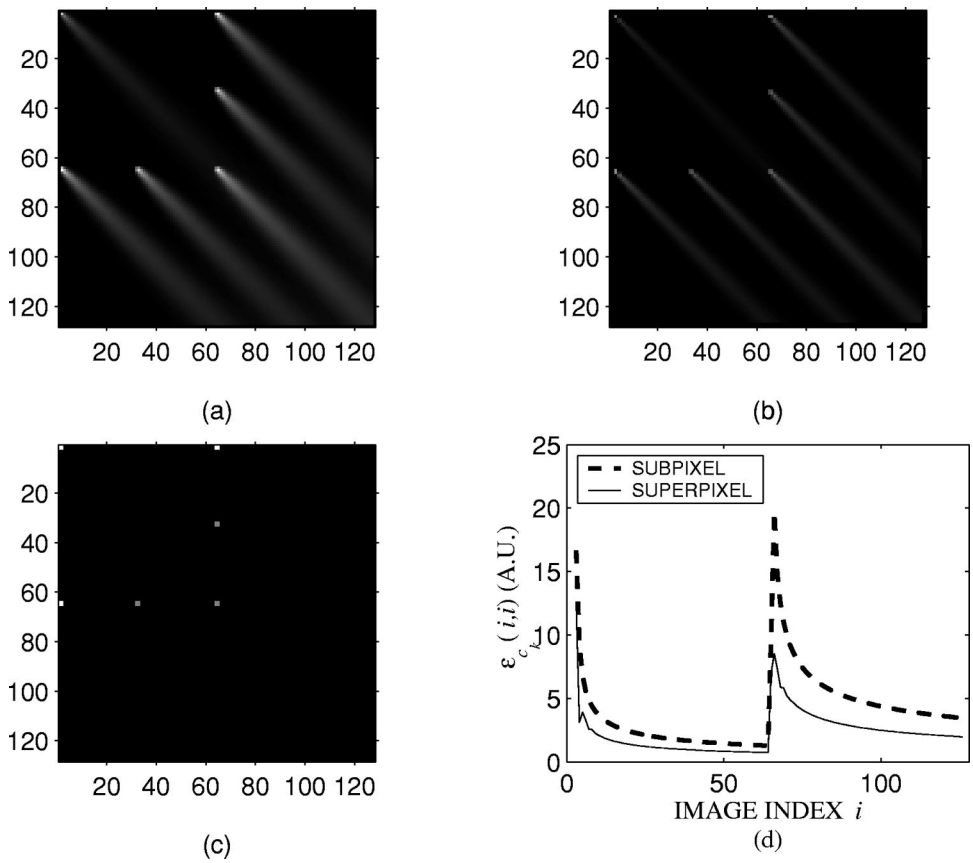

Fig. 5. Propagation of error: (a) subpixel 2D motion case for a shift of (0.5, 0.5), (b) superpixel 2D motion case for a shift of (1.5, 1.5), (c) frame 1 of the second test pattern image (the bright pixels indicate the nonzero values used to introduce residual nonuniformity and bilinear-interpolation error), (d) plot of the diagonal elements $c_k(i, i)$, $i = 1,2,...,128$, for the images in (a) and (b).

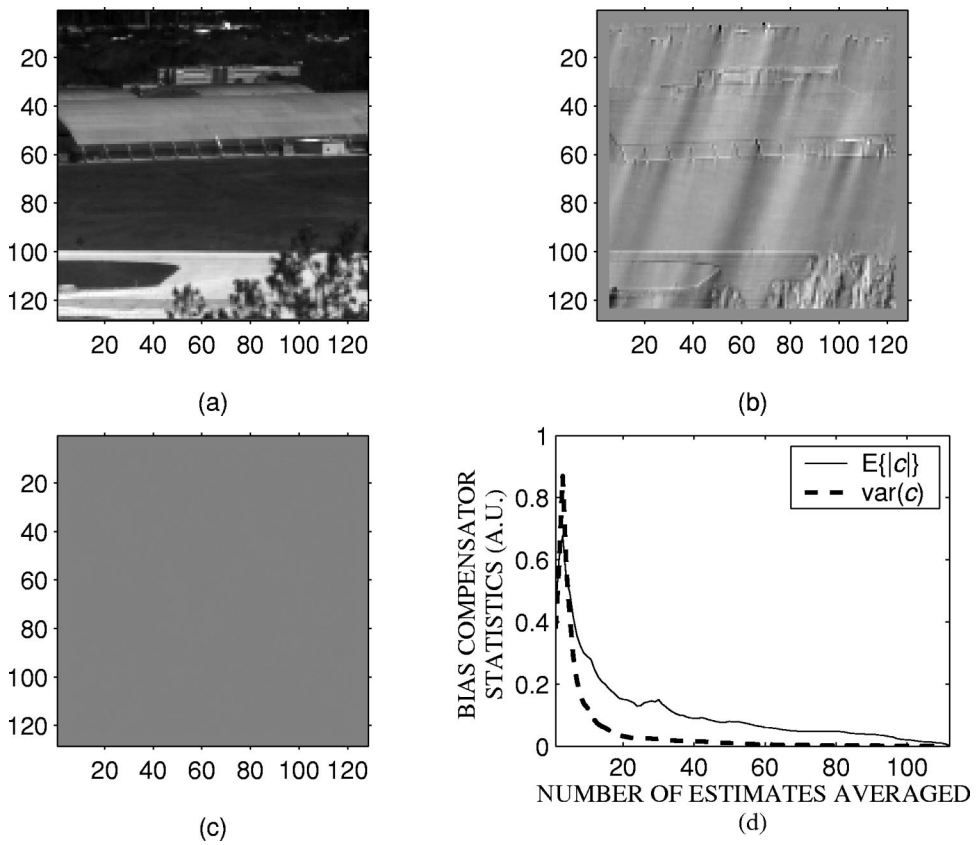

Fig. 6. (a) Image frame 119 from data set 1 after correction by the GASBA, (b) bias compensator estimates produced from the correction of frames 119 and 120 (linearly scaled to the full dynamic range), (c) bias compensator estimates after averaging 112 estimate matrices, (d) plot showing the mean and the variance of the bias compensator estimates as a function of the number of estimates in the average.

$$\epsilon_{c_k}(i,j) = -\sum_{m=m_0}^{i}\sum_{n=n_0}^{n_f}\sum_{l=l_0}^{l_f}\sum_{r=r_0}^{l_f}(-1)^{-(l_0+r_0)} \times B(p,q,l,r)\epsilon_{\Delta_k}(m,n)(-|\Delta\beta_k|)^l(-|\Delta\alpha_k|)^r, \quad (17)$$

where $m_0 = \max(2 + \lfloor\alpha_k\rfloor, i - 2[j - \lfloor\beta_k\rfloor] + 3)$, $n_0 = \max(2 + \lfloor\beta_k\rfloor, j - 2p)$, $l_0 = \max(0, q - p)$, $r_0 = \max(0, p - q)$, $l_f = \min(p, q)$, and $n_f = j - [p/2]$, where $[x]$ indicates the smallest integer greater than x. Although the error coefficients $B(p, q, l, r)$ can be computed, we have not been able to deduce a closed-form mathematical formula for them. Despite this, Eq. (17) is still useful in that it gives a meaningful description of the error propagation for this case. First note that each $\epsilon_{c_k}(i, j)$ term involves a smaller number of $\epsilon_{\Delta_k}(m, n)$ terms than in the 2D subpixel case. In this case, the m and n indices form a cone-shaped pattern rather than the rectangular pattern of the 2D subpixel case. We again find that the shift terms are largest in magnitude along the direction of motion. Note also that all shift terms are in the numerator and form a double alternating sum of increasing power, causing the error to be less than that in the 2D subpixel case.

Figures 5(a) and 5(b) depict the bias compensator estimates generated by the algorithm for the 2D subpixel and superpixel cases, respectively, using a second test pair (created similarly to that in the 1D case), of which the first image is shown in Fig. 4(c). The shifts used in the respective cases were (0.5, 0.5) and (1.5, 1.5) pixels. Figures 4(a) and 4(b) are scaled to the same dynamic range of [0, 22.2], where the ranges of the bias compensators are [0, 22.2] and [0, 12.5], respectively. Examining both images, we find that they have similar characteristics. As expected, the error has effectively been projected in both cases along a direction of −45°, consistent with Eqs. (15) and (17). We also find that the spread of the error in both cases is in the shape of a cone. Note that in the superpixel case the width of the cone is thinner than in the subpixel case. This is attributed to the fact that (1) the error damps out more quickly in the superpixel case on account of the fact that all the $\Delta\alpha_k$ and $\Delta\beta_k$ terms are in the numerator and (2) each error term involves a reduced number of $\epsilon_{\Delta_k}(m, n)$ terms.

To see the error projection patterns more clearly, we show in Fig. 5(d) a plot of $\epsilon_{c_k}(i, i)$ along the diagonal elements for $i = 1,...,128$ of Figs. 5(a) and 5(b). In both cases, the envelope of the error decreases quadratically from its initial peak value. The error curves peak a second time once another error is encountered. Also note the slight ringing near the peaks in the superpixel plot. This ringing is consistent with the double alternating sum of Eq. (17).

In summary, through the sets of images used in the study, we conclude that the effect of bilinear interpolation and residual nonuniformity error is less severe for the

case of superpixel 2D motion. Though it was shown that superpixel 1D motion yields better algorithm performance than subpixel 1D motion, both of these cases produce corrections that contain the undesirable column/row striping artifacts. Thus we conclude that the best corrections are those produced when only image pairs exhibiting 2D motion are used.

C. Improving Bias Compensator Accuracy

In this subsection, we study how averaging many bias compensator estimates, produced from different image pairs, reduces the overall effect of the above errors. Recall that this averaging is performed in step 6 of the algorithm description in Subsection 2.B. To perform this study, we first apply the GASBA to remove the nonuniformity in data set 1. Image frame 119 from this correction is displayed in Fig. 6(a). We next reapply the GASBA to this clean image sequence. Since the nonuniformity has been removed, the bias compensators produced from this second GASBA application should all be zero. Thus any nonzero bias compensators can be attributed to error. The bias compensators produced from the image pair for frames 119 and 120 are shown in Fig. 6(b), which is linearly scaled to the full dynamic range of $[-4.46, 3.59]$. The shift between these image frames was $(-0.257, 0.765)$ pixels. Note that the error pattern shows projections along a direction of $-108.5°$, which is consistent with the direction of motion.

Of the 512 frames in the image sequence, a total of 112 image pairs exhibiting 2D motion were found. These image pairs were then used to estimate the bias compensators, each resulting in compensator estimates similar to those of Fig. 6(b). The resulting compensator estimates were then averaged for each pixel (note that because of the dynamic perimeter sizes, some detectors have fewer than 112 estimates). The resulting averaged bias compensator estimates are displayed in Fig. 6(c), scaled to a dynamic range of $[-0.5, 0.5]$. The range of these averaged bias compensator estimates is $[-5.74 \times 10^{-14}, 5.14 \times 10^{-14}]$, or effectively zero as expected.

Finally, to study the rate at which the compensator errors converge to zero for this data set, we display in Fig. 6(d) the mean absolute error and the variance of the averaged bias compensator estimates as a function of the number of estimates in the average. As can be seen, the variance of the error is nearly zero after averaging just 20 estimates. After 100 estimates have been averaged, the mean absolute error and the variance are both essentially zero.

5. CONCLUSION

We have presented a novel generalization to a recently developed algebraic scene-based NUC algorithm. This new technique is able to estimate quantities that are used to compensate for bias nonuniformity by using pairs of image frames exhibiting arbitrary 1D or 2D global translational motion. The key step of the algorithm is to guarantee bias uniformity in the perimeter of each image pair by using the previously developed ASBA technique.[14] Then, with the use of these perimeter-unified image pairs, a modified version of the RASBA technique[15] is applied, allowing for image pairs containing arbitrary translational motion to be used to correct the interior pixels of the FPA.

The algorithm's ability to provide a high-quality NUC on real IR data, obtained from both cryogenically cooled and uncooled FPAs, was demonstrated despite the presence of gain nonuniformity. Moreover, the algorithm is able to perform these corrections in a shutterless manner, i.e., without the need for a blackbody calibration target. The effects of bilinear-interpolation error, e.g., that due to local motion, object deformation, etc., and of residual perimeter nonuniformity, arising from error in the ASBA compensator estimates, on the performance of the algorithm were also thoroughly studied. We determined that these errors were least harmful when the image pairs contained superpixel 2D motion. We also found that the generalized algorithm does not suffer from the typical striping artifacts present in the original ASBA technique when the motion is diverse, since the error is projected along many different directions in the 2-D case, rather than strictly along rows and columns. While these sources of error can significantly degrade algorithm performance, we demonstrated that these errors can be overcome when a sufficient number of compensator estimates are averaged in time. For example, for the 512-frame data set considered, these errors converged to zero after approximately 100 compensator estimates were averaged.

One of the strengths of the algorithm is its computational efficiency, lending itself to a real-time hardware-based application. An initial hardware design (not reported here) has been completed and, without any optimization, yields simulated corrections at a near-real-time speed of 14 frames per second. Future work will continue on the hardware optimization of this real-time implementation, which is specifically focused toward hand-held imaging applications.

ACKNOWLEDGMENTS

The authors thank Kamil Agi at K&A Wireless, LLC, and Ernest Armstrong at the U.S. Air Force Research Laboratory Sensors Directorate at Wright-Patterson Air Force Base, Ohio, for providing us with IR imagery. This project was partially supported by K&A Wireless, LLC, through a National Science Foundation Small Business Innovation Research (SBIR) Phase-I program (award 0319323).

Corresponding author Majeed Hayat's e-mail address is hayat@ece.unm.edu.

REFERENCES

1. G. C. Holst, *CCD Arrays, Cameras, and Displays* (SPIE Optical Engineering Press, Bellingham, Wash., 1996).
2. A. F. Milton, F. R. Barone, and M. R. Kruer, "Influence of nonuniformity on infrared focal plane array performance," Opt. Eng. (Bellingham) **24**, 855–862 (1985).
3. D. L. Perry and E. L. Dereniak, "Linear theory of nonuniformity correction in infrared staring sensors," Opt. Eng. (Bellingham) **32**, 1853–1859 (1993).
4. P. M. Narendra, "Reference-free nonuniformity compensation for IR imaging arrays," in *Smart Sensors II*, D. F. Barbe, ed., Proc. SPIE **252**, 10–17 (1980).

5. P. M. Narendra and N. A. Foss, "Shutterless fixed pattern noise correction for infrared imaging arrays," in *Technical Issues in Focal Plane Development*, W. S. Chan and E. Krikorian, eds., Proc. SPIE **282**, 44–51 (1981).
6. J. G. Harris, "Continuous-time calibration of VLSI sensors for gain and offset variations," in *Smart Focal Plane Arrays and Focal Plane Array Testing*, M. Wigdor and M. A. Massie, eds., Proc. SPIE **2474**, 23–33 (1995).
7. J. G. Harris and Y. M. Chiang, "Nonuniformity correction using constant average statistics constraint: analog and digital implementations," in *Infrared Technology and Applications XXIII*, B. F. Andersen and M. Strojnik, eds., Proc. SPIE **3061**, 895–905 (1997).
8. M. M. Hayat, S. N. Torres, E. E. Armstrong, and B. Yasuda, "Statistical algorithm for non-uniformity correction in focal-plane arrays," Appl. Opt. **38**, 772–780 (1999).
9. S. N. Torres and M. M. Hayat, "Kalman filtering for adaptive nonuniformity correction in infrared focal plane arrays," J. Opt. Soc. Am. A **20**, 470–480 (2003).
10. W. F. O'Neil, "Dithered scan detector compensation," in *Proceedings of the 1993 International Meeting of the Infrared Information Symposium Specialty Group on Passive Sensors* (Infrared Information Analysis Center, Ann Arbor, Mich., 1993).
11. W. F. O'Neil, "Experimental verification of dithered scan nonuniformity correction," in *Proceedings of the 1996 International Meeting of the Infrared Information Symposium Specialty Group on Passive Sensors* (Infrared InformationAnalysis Center, Ann Arbor, Mich., 1997), Vol. 1, pp. 329–339.
12. W. F. O'Neil, "Dither image scanner with compensation for individual detector response and gain," U.S. Patent No. 5,514,865.
13. R. C. Hardie, M. M. Hayat, E. E. Armstrong, and B. Yasuda, "Scene-based nonuniformity correction using video sequences and registration," Appl. Opt. **39**, 1241–1250 (2000).
14. B. M. Ratliff, M. M. Hayat, and R. C. Hardie, "An algebraic algorithm for nonuniformity correction in focal-plane arrays," J. Opt. Soc. Am. A **19**, 1737–1747 (2002).
15. B. M. Ratliff, M. M. Hayat, and J. S. Tyo, "Radiometrically accurate scene-based nonuniformity correction for array sensors," J. Opt. Soc. Am. A **20**, 1890–1899 (2003).
16. R. C. Hardie, K. J. Barnard, J. G. Bognar, and E. A. Watson, "High-resolution image reconstruction from a sequence of rotated and translated frames and its application to an infrared imaging system," Opt. Eng. (Bellingham) **37**, 247–260 (1998).